Experimental Mechanics (2007) 47:625–635
DOI 10.1007/s11340-006-9025-5

Aerodynamic Coefficients and Deformation Measurements on Flexible Micro Air Vehicle Wings

R. Albertani · B. Stanford · J.P. Hubner · P.G. Ifju

Received: 12 July 2006 / Accepted: 28 November 2006 / Published online: 3 February 2007

Abstract This paper documents the elastic deformations and corresponding aerodynamic coefficients of flexible wings used for micro air vehicles (MAVs). These low-aspect ratio wings, developed and fabricated at the University of Florida, incorporate an elastic latex membrane skin covering a thin carbon fiber skeleton. The wings were tested in a unique low-speed wind tunnel facility integrating a visual image correlation (VIC) system with a six-component strain gauge sting balance. Model characteristics are presented, along with the appropriate specimen preparation techniques and wind tunnel instrumentation. The static response characteristics, including full-field displacements and plane strain measurements, for three distinct MAV wing designs are presented. The full-field deformation results show how passive wing flexibility preferably affects aerodynamic performance when compared to a rigid model of similar geometry.

Keywords VIC; visual image correlation · MAV; micro air vehicle · Wind tunnel · Membrane wing · Flexible wing

R. Albertani (✉)
Research & Engineering Education Facility (REEF),
University of Florida,
Shalimar, FL, USA
e-mail: ralb@ufl.edu

B. Stanford · P.G. Ifju (SEM member)
University of Florida,
Gainesville, FL, USA

J.P. Hubner (SEM member)
University of Alabama,
Tuscaloosa, AL, USA

Introduction

MAVs are a class of aircraft with a maximum size of 150 mm, and are capable of operating at speeds of 15 m/s or less [1]. The concept is for a small, inexpensive and expendable (if required) platform to be used for missions of surveillance and measurements in situations where larger vehicles are not practical or too expensive. Such missions can include low-altitude operations in battlefield, urban, or wildlife applications. Payloads may consist of video cameras, chemical sensors and communication devices. Figure 1 illustrates a typical operational University of Florida MAV with a 150 mm wingspan.

There are numerous technical challenges associated with designing and creating very small flying vehicles including a precipitous reduction in aerodynamic efficiency as the Reynolds number drops below 100,000—the typical flight regime for MAVs. Other critical areas are the guidance, navigation and control (GNC), the design of efficient and reliable propulsion systems, and the management of environmental disturbances such as wind gusts. Fixed-winged MAVs generally employ a low-aspect ratio (LAR) design wing; these wings are characterized by a three-dimensional flow field and by a delayed stall to higher angles-of-attack (AOA). Studies on LAR wings date back to the late 1930s [2, 3] where tests showed discrepancies between pre-stall experimental results and the predicted lift-curve slope found using Prandtl lifting-line theory [4]. Later studies by Hoerner [5] investigated the nature of the three-dimensional flow field and the extent of the developing vortex system over LAR wings. More recent research by Mueller's group [6–8] proved the importance of camber and wing shape, indicating that the inverse-Zimmerman shape was superior for low Re flow.

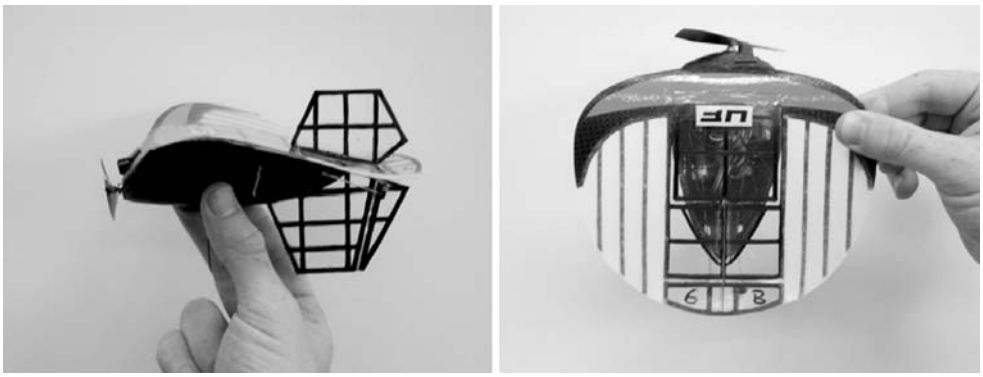

Fig. 1 Typical MAV with a wingspan of 150 mm and equipped with a video camera

While these previous investigations have focused on rigid wings, the design developed for the University of Florida MAV program, shown in Fig. 2, employs passive flexibility. The wings are constructed of a carbon fiber skeleton and a thin extensible rubber membrane [9, 10]. Wind tunnel investigations and flow diagnostic tests focusing on aerodynamic coefficients and stability derivatives [11–13] have been performed to document global force-moment behavior. Numerical attempts using computational fluid dynamics and finite element analysis [14, 15] have focused on the fluid-structure interactions and the prediction of leading-edge separation. Experimental results were not available to validate the predicted wing's elastic deformation. Previous efforts to measure wing deformation included projection moiré interferometry (PMI) [16–18], videogrammetry [11, 18, 19], and finite element methods [20]. While PMI provided useful out-of-plane displacements, it does not yield in-plane strains. Photogrammetric techniques only produced low spatial-resolution data sets and would require interpolation techniques to determine displacements for higher density grids. High spatial resolution data, as well as material properties, are necessary to accurately model the fluid-structure interactions of a deformable flying structure, either in vehicles or biological systems [21–23].

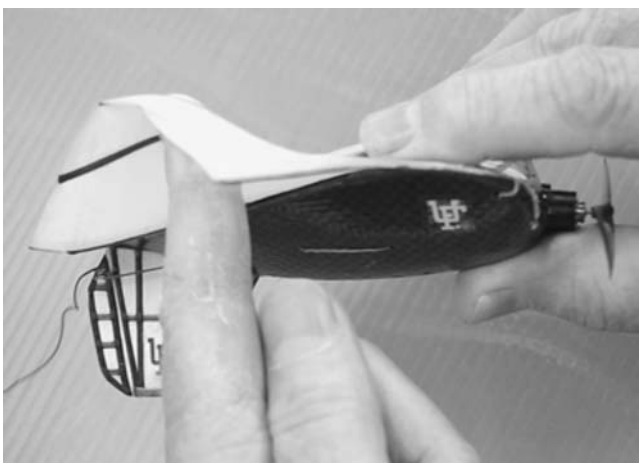

Fig. 2 Flexibility of the MAV wing

This paper documents the use of visual image correlation [24–26] to obtain high-resolution elastic deformation (displacements and in-plane strains) on a series of flexible LAR wings in a low-speed wind tunnel. The experimental procedure is first presented, highlighting key details of the instrumentation and model preparation. Next, aerodynamic and deformation results corresponding to two flexible wing designs of differing structural characteristics, subjected to a variety of flight conditions are presented and discussed. The corresponding aerodynamic force and moment data are compared to data garnered from a rigid wing of nominally identical geometry, in order to further elucidate the effects of the wings' elastic flexibility for MAV applications.

Experimental Setup

Wind Tunnel and Related Instrumentation

All tests were performed at the University of Florida's open-circuit, low-speed, low-turbulence wind tunnel. The wind tunnel has a 0.9 m×0.9 m×2 m test section with optical access from the sidewalls and the ceiling. Typical testing Reynolds numbers, based on wing chord geometry and flow speeds, range between 50,000 and 150,000. A 10 mm diameter, six-component (five forces and one moment), sting balance was used for aerodynamic force (lift, drag, side) and moment (roll, pitch, yaw) measurements. Figure 3 illustrates the installation of a flexible micro air vehicle wing in the wind tunnel. The sting balance is attached to a pitch-adjustable arm which is used to set model AOA. The wind tunnel flow dynamic pressure and temperature were continuously monitored for free stream velocity calculations. Tunnel speed, model inclination and force/moment measurements were set and/or acquired using a dedicated multi-channel data acquisition system and in-house software developed in LabVIEW.

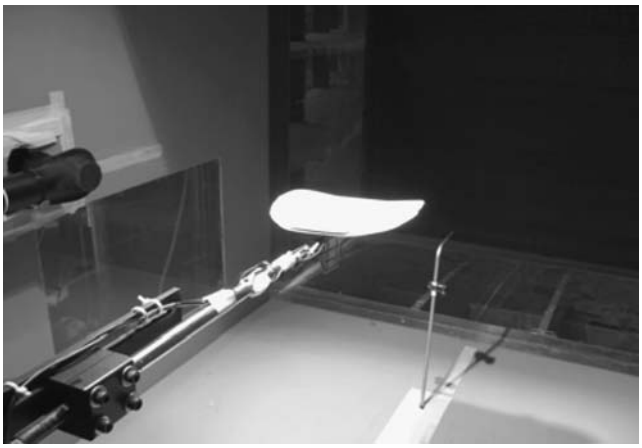

Fig. 3 MAV wing installed in the wind tunnel for testing

Visual Image Correlation

A VIC system was used to measure the wing geometry, displacements, and plane strains [27]. In order to capture the three-dimensional features of the models, synchronized twin cameras, each looking from a different viewing angle, were installed above the wind tunnel ceiling, as shown in Fig. 4. As the cameras must remain stationary throughout the experiment, a mounting bracket was constructed around the wind tunnel test section to prevent the transmission of vibrations. The operating principle of the VIC technique is to determine the displacements of a specimen under load by tracking the deformation of a random speckle pattern previously applied to its surface. The random pattern is digitally acquired by the cameras before and during loading (wind-off and wind-on conditions). Relative movement of the speckle pattern, and hence surface displacements, are determined by maximizing the normalized cross-correlation score between the two images. The calibration of the two cameras (to account for lens distortion and determine pixel spacing in model coordinates) is the ab initio step, which permits the determination of the corresponding image locations from views in the different cameras. The reconstruction of the 3D features of the specimen is then possible.

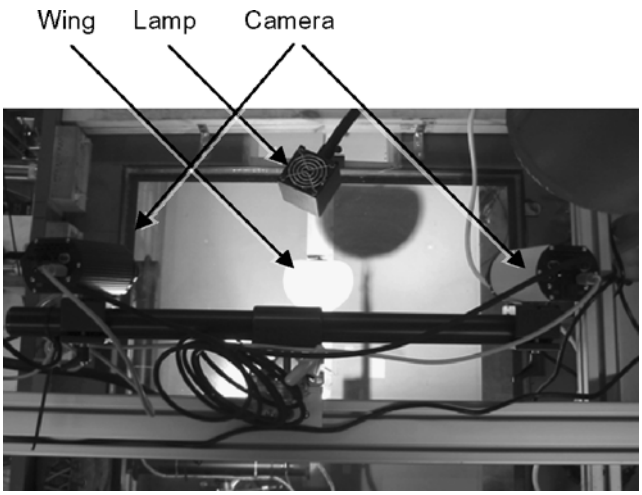

Fig. 4 View from the top of the wind tunnel with the two lights, the two cameras and the MAV wing model

Optical access into the test section was through a float glass window. The results of conducting visual image correlation with a glass interface between the cameras and the specimen have been studied [28], with little benign effects reported. Furthermore, the cameras were initially calibrated through the window to ensure minimal distortion. Two continuous 250 Watt lamps illuminated the model, enabling the use of camera exposure times of 5–10 ms. The energy emitted by the lights, a potential hazard for the specimen (particularly the thin membrane skin, whose elastic properties are known to degrade in adverse conditions), was not a concern due to the cooling effect of the wind tunnel flow rates, typically from 8 to 13 m^3/s.

Although the accuracy of the VIC system can be estimated via a pure translation and/or rotation experiment for a nominally planar object, an alternate technique was favored in order to closely emulate the experiment in the wind tunnel. Furthermore, the authors had every confidence in the off-the-shelf VIC's ability to accurately handle rigid body movements. The objective of the tests was to check the system's ability to handle small, out-of-plane displacements simultaneously with small in-plane strains wherein the displacement magnitude is significantly smaller than the length scale of the deforming structure. In order to simulate the deformation patterns that we would expect over a MAV wing, a known displacement was applied to a structure, and then compared with the field concurrently measured by way of image correlation. A thin latex membrane, identical to the material used for the wing skin of the MAVs, was moderately stretched and fixed to a rigid aluminum ring with an inner diameter of 100 mm. The center of the membrane circle was then indented with a rigid steel bar with a spherical head of 8 mm diameter. The bar was moved against the membrane by a micrometer with minimum increments of 0.02 mm. A commanded membrane displacement (via the micrometer) of 5 mm was under-predicted by VIC by 0.00104 mm. Conversely, a commanded displacement of 0.1 mm was over-predicted by 0.0017 mm. The average error computed across the range of displacements was ±0.003 mm [29], suitable for MAV geometries investigated in this study.

Model Preparation

The preparation of the specimen for VIC analysis is relatively straight forward, but requires attention to some important details, especially the color choice of the wing's structure with respect to the target surface (to blend with the

wing skin). The finish of the skin must be diffuse to minimize or eliminate noise during image processing. The following steps describe the model preparation.

Step 1: The MAV's wing skeleton is constructed out of carbon fiber composites [10]. After the composite skeleton has cured, the top surface is coated with a light-colored paint, Fig. 5(a), similar to the color of the membrane skin. This minimizes the visibility, and negative optical effects, of the wing battens through the partially transparent wing skin.

Step 2: The wing skin, consisting of thin, lightly colored and partially transparent latex rubber is speckled with a flat black paint, as illustrated in Fig. 5(b). Numerous speckling applicators are appropriate; the jet from an enlarged spray-paint nozzle is used here. After the paint has dried, a coat of dulling spray is applied to the same side of the latex. Each paint speckle, while relatively brittle (compared to the extensible latex) has a small average diameter (less than 0.5 mm) and is generally isolated from adjacent speckles. Thus the speckle pattern is not thought to significantly change the mechanical behavior of the latex skin. If information concerning the state of the pre-strain in the MAV wing is desired, a picture of the latex sheet is captured, for later use as a reference in the VIC system.

Step 3: The latex is stretched out around a frame, and the perimeter is retained to hold the desired tension. Spray mount adhesive is applied to the painted side of the carbon fiber skeleton wing; the wing is then attached to the clean side of the latex. After the spray adhesive dries, the excess latex rubber is trimmed away. The completed wing model, shown in Fig. 5(c), is now ready for testing in the wind tunnel.

The results from three MAV wings, extensively flight tested and implemented in practical missions [31] are discussed in this paper. All three wings were manufactured from the same CNC mold, and thus have the same nominal geometry with a wing area of 1.780E-02 m^2 estimated from the numerical model of the wing. The root chord length (the distance from the leading edge to the trailing edge at the center of the wing) is 130 mm, the wing span is 150 mm resulting in an aspect ratio of 1.264; the camber is 3.5 mm. Structurally the wings are quite distinct from one another; the three designs are detailed in Fig. 6. The rigid wing (R) is constructed from three plies of bi-directional plain weave carbon fiber composites, with fibers running in the ±45° directions. The term "rigid" is slightly inaccurate, as the stiff laminate can be expected to show some, albeit inconsequential, deformation as a response to aerodynamic loading. The batten reinforced wing (BR) is built from two plies of the same plain-weave carbon fiber in the central portion and leading edge of the wing. Thin strips of two-layer uni-directional carbon fiber laminates (battens) are evenly spaced on either side of the wing. A 0.2 mm thin latex membrane is adhered to the surface of this skeleton. The perimeter reinforced wing replaces the batten reinforcement with a curved strip of plain weave carbon fiber that traces the perimeter of the wing, connecting the leading edge to the trailing edge. As before, the membrane is attached to this surface.

Test Procedure

The objective of the experiment was to determine the deformation of the wings under steady aerodynamic loads, at different AOAs and free stream velocities, while acquiring simultaneous aerodynamic force data. Each AOA required a separate wind-off reference image: failure to do so would add rigid body motions (as the model moves sequentially from one AOA to the next) into the displacement fields. The images taken for VIC (reference or otherwise) were of the final assembled wing including the pre-stretched skin, therefore pre-strain in the membrane is not included in the strain field measured from the wing. The measured strain fields presented in this work are strains caused exclusively by aerodynamic loading. This condition needs to be carefully considered in the evaluation of the results, since the areas of relaxation of the pre-existing

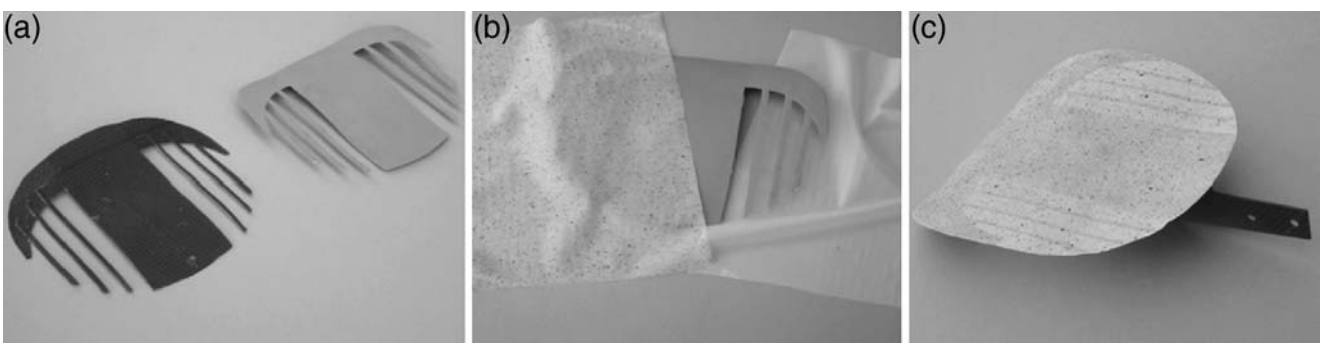

Fig. 5 (**a**) MAV wings without and with paint. (**b**) Latex skin before and after speckling. (**c**) Latex skin adhered to the carbon-fiber wing

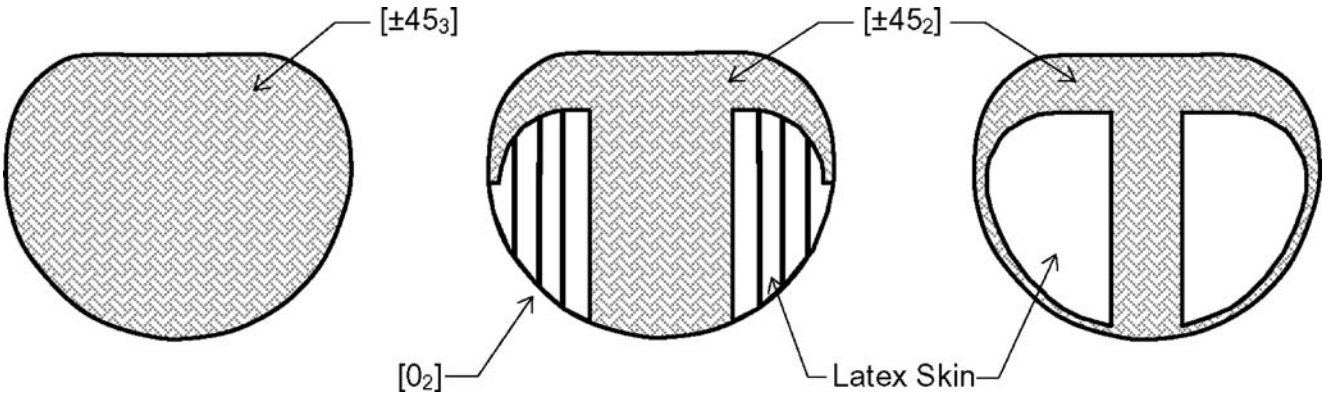

Fig. 6 Three distinct MAV wing structures, from *left* to *right*: the rigid wing (R), the batten reinforced wing (BR) and the perimeter reinforced wing (PR)

tension will generate areas of "virtual" compression in the skin (the thin membrane cannot support compressive strain: it will merely wrinkle). In order to obtain the absolute state of strain in the latex an alternative procedure would be to take images of the latex before and after it is adhered to the carbon fiber wing's structure. The images will be processed through the VIC system and the results stored for further analysis. Next the wind tunnel tests will be performed in the usual way, including a new reference picture in wind-off condition at each AOA with the corresponding win-on image of the deformed structure. At that point the pre-strain field can easily be interpolated onto the wing surface, and the absolute state of strain at each node could be calculated, if required. The pre-stress conditions of the wing's membrane were not relevant to the scope of this work, and are therefore not considered. The procedural steps were:

1. Take a picture of the model at the set angle, with the wind off.
2. Start the wind tunnel and wait for stable conditions.
3. Take the picture of the deformed wing, and record the aerodynamic loads simultaneously.
4. Stop the wind tunnel and move the model to the next AOA.

This sequence was repeated for a range of AOA, typically from 4° up to 36°. The procedure was repeated for the selected free stream velocities, ranging between 8 and 13 m/s.

Test Results and Discussion

Aerodynamic Characteristics of MAV Wings

Aerodynamic loads were measured over AOA sweeps from 4° to 36° with no model yaw. Thus the side forces were effectively zero until stall conditions and so only longitudinal forces are presented. Figure 7(a) plots the lift coefficient versus AOA for the three wing geometries at a free stream velocity of 13 m/s. Figure 7(b) illustrates the slope of the linear portion of these curves as a function of airflow speed. Typical of LAR wings, the average lift curve slopes (~0.05/deg) are shallower than thin high aspect ratio wings or 2D airfoils (~0.11/deg). The LAR nature of the wings under consideration provides noticeably Fig. 7(a) higher stall angles than their high aspect ratio counterparts. For a given AOA, the lift coefficient of the perimeter reinforced wing is substantially larger than the rigid and batten reinforced models. This is due to the billowing of the

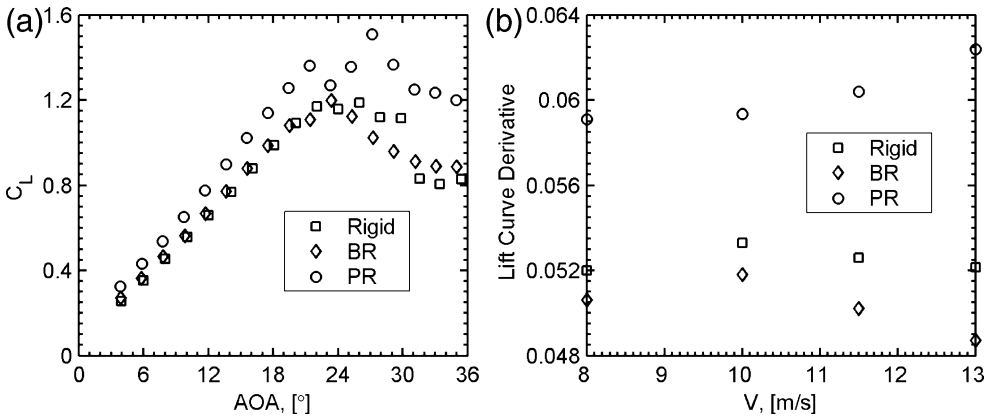

Fig. 7 (**a**) Lift coefficients at a free stream velocity of 13 m/s. (**b**) The slope of the lift curve found at different free stream velocities

membrane in between its carbon fiber perimeter effectively increasing the camber and lift. The lift of a batten-reinforced wing is similar to that found with the rigid wing. This is thought to be a function of two competing factors. The passive deformation along the trailing edge of a BR wing, termed "adaptive washout," decreases the local angle of attack along the wing, and thus the lift. However, the camber of a BR wing will be shown to slightly increase with wing deformation, which offsets the loss in lift. The slope of the lift curve seen in Fig. 7(b), an important factor that is directly related to the wing's ability to handle vertical gusts (or similar environmental disturbances), is found to be lowest for the BR wing, regardless of free stream velocity. This is indicative of the adaptive washout built into the wing for gust alleviation.

The plots depicted in Fig. 8(a) display the wings' polar diagrams lift coefficient versus drag coefficient. All data in Fig. 8 is given for the three wings tested at 13 m/s. As neither flexible wing is expected to deform to an optimal aerodynamic shape when subjected to aerodynamic loading (passive optimum aeroelastic shaping was not the scope of this work), both flexible wings (PR and BR) show a slight drag penalty compared to their rigid counterpart Fig. 8(a). The perimeter reinforced wing is particularly inefficient: the billowed shape of the membrane creates a tangent discontinuity in the wing surface at the membrane/carbon fiber boundary (as will be detailed in the next section). The presence of battens, with their relatively streamlined shape, provides a BR wing with intermediate drag values. Indeed the rigid wing exhibited a higher lift to drag ratio, which suggests a better aerodynamic efficiency. A deformable wing, however, can be expected to have an intrinsic benefit: a portion of the energy that would normally be lost to the wing-tip vortices and wake, downstream of the MAV, now is stored as elastic strain energy in the wing's structure, an advantage well known and exploited by biological systems [22, 32].

The longitudinal static stability, detailed via the pitching moment coefficient about the 25% of the root chord, depicted in Fig. 8(b), can be considered a primary target of design improvement from one generation of vehicles to the next. The vehicles are highly sensitive to the longitudinal position of the center of gravity (CG). The range of flyable CG locations is generally a few percent of the mean aerodynamic chord (MAC), less than 10 mm long in the case of MAVs. To meet this requirement is a truly demanding design challenge. The negative slope of all three curves in Fig. 8(b) indicates that the wings are longitudinally statically stable: sudden disturbances in pitch create a moment that returns the wing to the initial position (a negative moment corresponds to a nose-down rotation of the wing). The flexible wings show a substantial improvement in the slope of the pitching moment curve. The derivative values of the BR wing are approximately double those of the rigid, while the PR values can be as much as triple. This is a result of the change in the position of the camber of the membrane wing. The PR wing also displays an extended linear portion of the pitching moment curve, achieving a more benign longitudinal control at higher AOAs.

VIC Results

Figure 9 illustrates typical VIC results for the surface of a perimeter reinforced wing at 22° AOA and at a flow velocity of 13 m/s. The billowed shape of the wing due to the aerodynamic pressure field is clearly evident. The coordinate system used for the current work is attached to the wing, as depicted in Fig. 9, wherein the origin corresponds to the centroid of the wing surface. The displacement field (u, v, and w) is found by subtracting the deformed surface from the reference surface. A post-processing option involves the calculation of the in-plane strains (ε_{xx}, ε_{yy}, and ε_{xy}). The VIC software performs the above by mapping the displacement field onto an unstructured triangular mesh, and conducting the appropriate numerical differentiation. Presentation of results will focus on the w displacements, rather than the in-plane motion

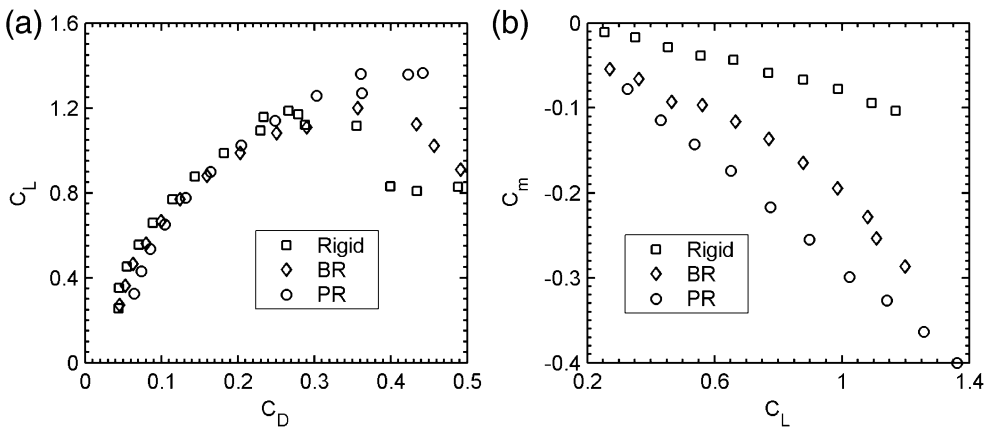

Fig. 8 (**a**) Drag polar found at a free stream velocity of 13 m/s. (**b**) The longitudinal stability of the three wings at a free stream velocity of 13 m/s

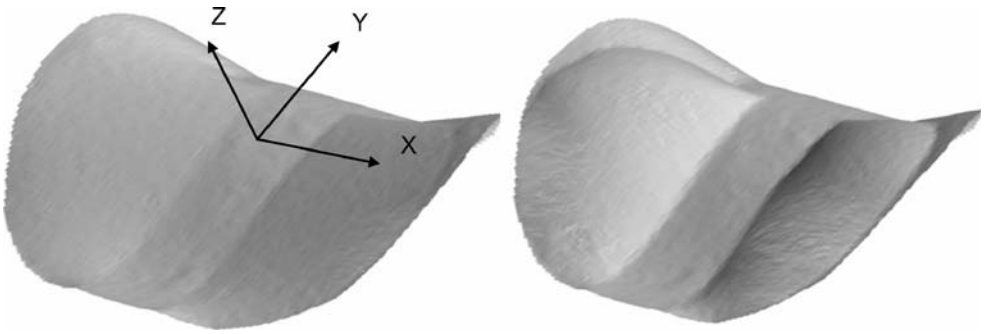

Fig. 9 Undeformed surface of a PR wing at 22° AOA (*left*), as measured by VIC. Deformed surface caused by aerodynamic loads at 13 m/s (*right*)

(u and v) for three main reasons: first, the MAV's thin carbon fiber skeleton is several orders of magnitude more compliant in the out-of-plane direction than the in-plane (this is not true for the membrane skin, however). Secondly, changes in local AOA and camber (mostly governed by w displacements) greatly influence the aerodynamics of the wing, as detailed in the preceding section. Finally, rigid body motions originating from the MAV's mounting system and sting balance predominately affect the w displacements and must be taken into account during the post processing.

Figure 10 presents the w displacements and in-plane strains for a batten reinforced wing at 12° AOA and 13 m/s. The thin hatched stripe drawn over the displacement contour (upper left) illustrates the locations that are fixed to a holder for connection with the wind tunnel's balance arm. The wing is effectively rigid along this fixture line, and nonzero out-of-plane displacements (~0.7 mm) indicate the aforementioned rigid body motions. These motions are thought to primarily originate from the flexibility of the strain-gauge sting balance that connects the MAV to the rig's arm. These rigid body motions can be easily corrected for, but are left in Fig. 10 for demonstration purposes. The corresponding strain fields are naturally unaffected by such motion.

The primary deformation shape is found at the outward trailing edge of the wing, where the battens are forced to bend upwards due to aerodynamic loading (this is the primary mechanism for adaptive washout). The change in shape is relatively small ($W_{max}/c \sim 0.03$, where c is 130 mm, the root chord), but as inferred in the preceding section, can have a dramatic effect on the aerodynamics. A second region of significance is the appreciable displace-

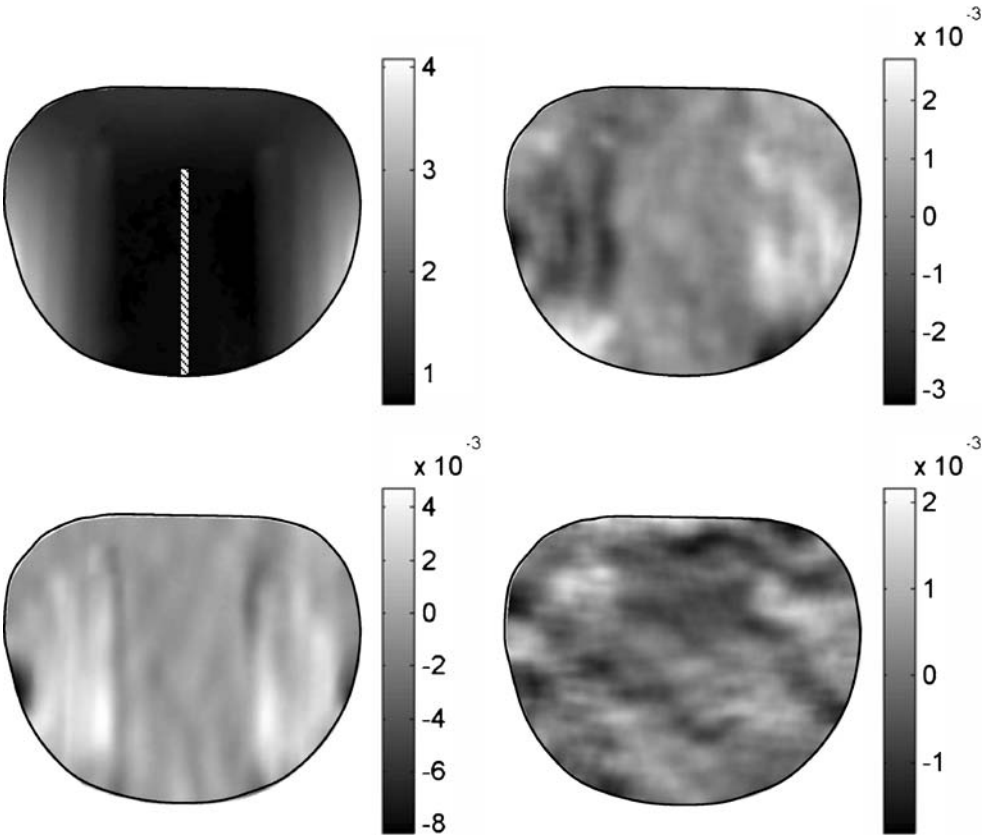

Fig. 10 Deformations of a batten reinforced wing at 12° AOA, and 13 m/s. The contour variables are, in *clockwise* order from *top left*, w displacement (mm), shear strain, in-plane strain parallel to the flow, and in-plane strain perpendicular to the flow. Vertical stripe in the *upper left* plot indicates location where MAV is fixed to a holder

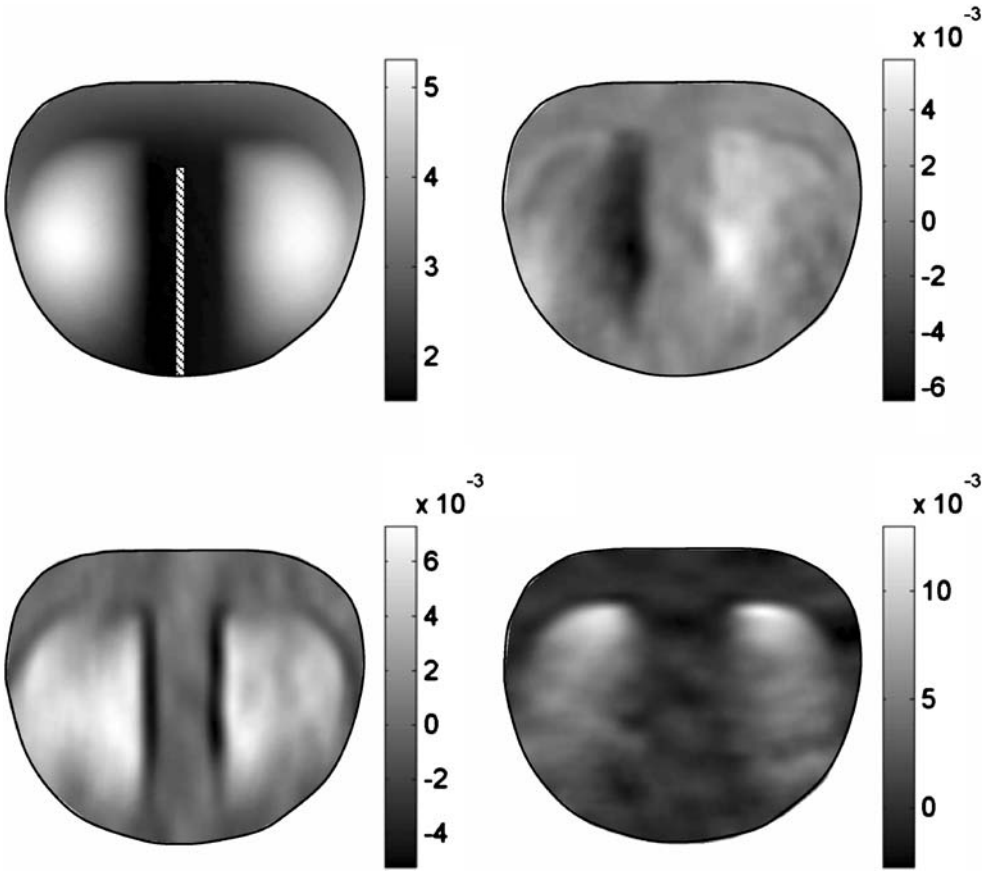

Fig. 11 Deformations of a perimeter reinforced wing at 22° AOA, and 13 m/s. The contour variables are, in *clockwise* order from *top left*, *w* displacement (mm), shear strain, in-plane strain parallel to the flow, and in-plane strain perpendicular to the flow. Vertical stripe in the *upper left* plot indicates location where MAV is fixed to a holder

ment at the carbon fiber wing tips. The VIC system can also detect the membrane's shape as it billows out between each batten. The majority of the strain in the thin membrane skin is in the direction perpendicular to the battens (ε_{xx}) and in shear (ε_{xy}). The battens prevent appreciable deformation in the chord direction (ε_{yy}). Interestingly enough these strain readings are relatively small and noisy. The strain resolution of the VIC system, under the current conditions, is estimated at 1000 $\mu\varepsilon$.

The pockets of negative strain at the trailing edge of each wing tip, illustrated in Fig. 10, are counter-intuitive for a thin membrane and are probably generated by numerical

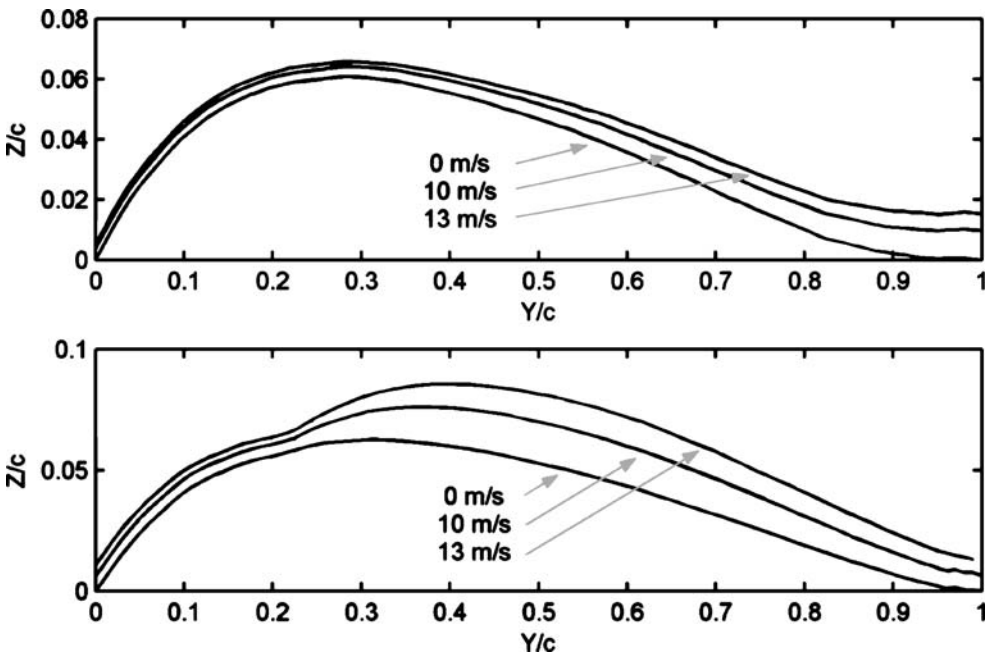

Fig. 12 Wing section profiles at 2X/*b*=0.67, for a BR wing (*top plot*) and a PR wing (*bottom plot*) at 16° AOA and in wind-off conditions and two wind tunnel flow speeds (10 and 13 m/s)

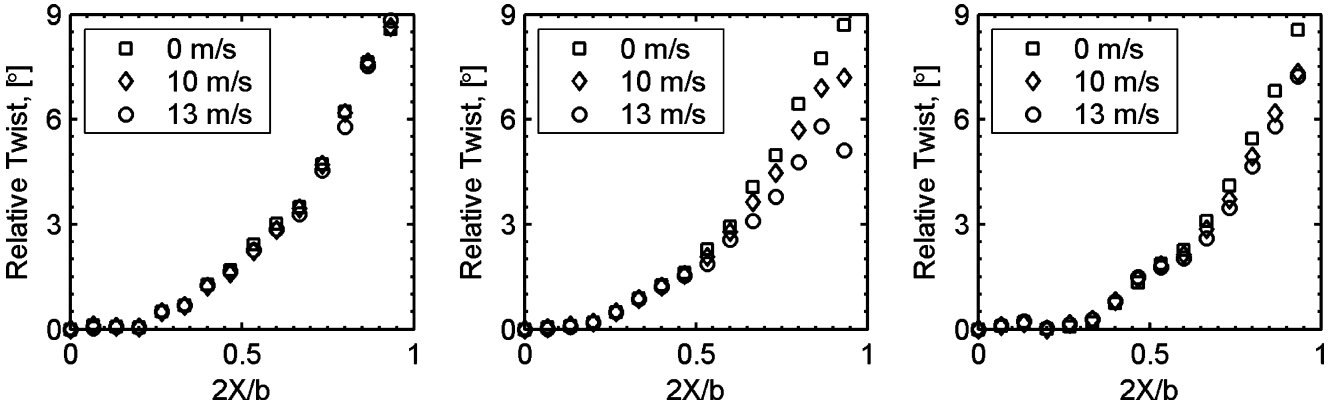

Fig. 13 Relative twist angle, i_w, along the semispan of a rigid wing (*left*), a BR wing (*center*), and a PR wing (*right*) at 12° AOA

differentiation errors. In order to explain the above conclusion we need to elucidate the physics of such wings in the interested region. For low aspect ratio wings a significant part of lift is generated by wing tip vortices, which can generate a local important suction. Furthermore, the interested area of the membrane wing is not subjected by the pre-tension and a steady vibration was observed at medium and high AOA. The vibrations were estimated by numerical methods [30] to have a frequency of approximately 100 Hz. The above factors along with the relevant deformations due to the washout effect may make the numerical differentiation scheme used by the VIC to solve the Lagrangian strain operator extremely susceptible to errors, notwithstanding the invariant properties of the operator. The numerical errors are not present in the steady parts of the wing. The system is able to measure a small bending compressive strain (−1500 $\mu\varepsilon$ in the chord direction) in the carbon fiber leading edge.

A similar plot is shown in Fig. 11 depicting the deformations of a perimeter reinforced wing at 22° AOA at a velocity of 13 m/s. As in the BR wing, rigid body motions are present. The major deformation shape is now the billowing of the membrane skin, changing the camber and therefore greatly affecting the aerodynamics, although deformation is again relatively small ($W_{max}/c \sim 0.04$). The thin curved carbon fiber strip that serves as the perimeter also shows substantial bending. The absence of battens allows for a full two-dimensional state of strain. Whereas the BR wing displayed negligible strain in the chord direction, the PR wing shows large values (14,000 $\mu\varepsilon$) at the membrane/carbon fiber boundary. A small bending compressive strain in the chord direction is again detected in the carbon fiber leading edge. The bottom left part of Fig. 11 also shows two areas of negative strain at the root chord. It was determined that the source was a creep phenomenon within the bonding of the pre-stressed latex to the carbon fiber. Therefore the results show the relaxation of the pre-stretched membrane.

To further interpret the wing deformation, the local chordwise (Y direction) shape or wing section profile, is plotted in Fig. 12 at a location 50 mm (2X/b=0.67, where b is the wingspan) from the wing's centerline. Results are given for both a BR and a PR wing; the testing conditions are at 16° AOA and wind-off, 10, and 13 m/s free stream velocity. For all wing profiles, the leading edge is on the left. From the deformations of the BR wing, Fig. 12 top, it can be observed that the basic airfoil shape does not change significantly for different flight speeds. The adaptive washout or substantial rotation of the wing section about the leading edge evident from the figure, provides the superior lift slopes and stall angles illustrated previously in Fig. 7. Minor changes in camber and camber location were

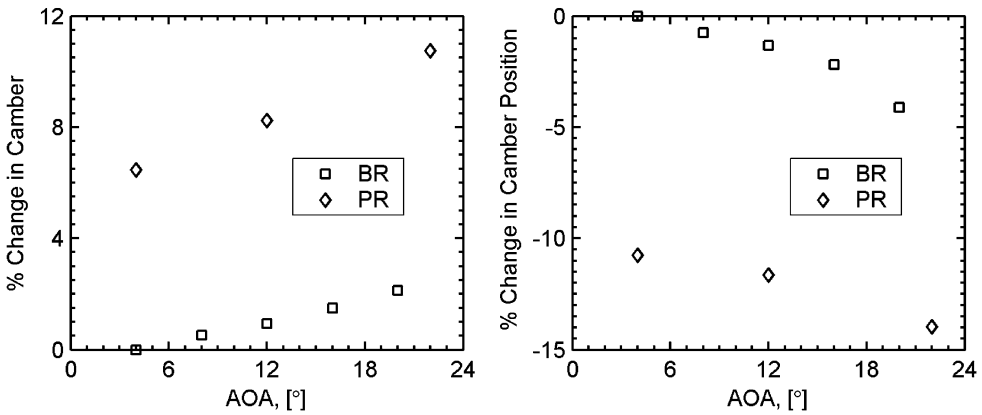

Fig. 14 Change in camber (*left*) and camber position (*right*) at the spanwise section 2X/b= 0.67, for 13 m/s

also observed. Conversely, the PR wing demonstrates negligible washout, Fig. 12 bottom, but substantial changes in shape. Notably, both the camber and its position are functions of the free stream velocity due to the billowed membrane. A discontinuity in wing shape at the membrane/carbon fiber boundary ($Y/c \sim 0.02$) is evident and is plausibly responsible, in part, for the drag increase of a PR wing Fig. 8(a) compared to the other wings.

The rotation of the local chordline is called geometric twist. The spanwise distribution of the relative twist angle, or angle of incidence i_w, between the root chord and the local chord is given in Fig. 13. Results are illustrated for the rigid, BR and PR wings (left to right, respectively) at 12° AOA. As a baseline, the rigid wing plot indicates the amount of geometric twist incorporated into the nominal design and therefore in the mold. As postulated above, increasing the wind velocity does not cause appreciable twisting (or other deformation) in the rigid wing. The adaptive washout of the BR wing allows for a significant decrease (as much as 4°) in the relative twisting angle with increasing wind speeds. In addition to the geometric twist, the shape of the wing section can change in the spanwise direction; this is defined as aerodynamic twist. The change in camber size and position is detailed in Fig. 14, for both flexible wings flying at 13 m/s. Results are given at the same spanwise location ($2X/b=0.67$). For the BR wing, the maximum vertical distance between the wing surface and the local chordline at a specific spanwise location (camber) increased moderately as AOA increased. Additionally, the chordwise location of the camber moved toward the trailing edge. The PR wing exhibits similar trends in camber and camber's position, albeit with significantly larger magnitudes and greater benefits to the wing's lift and static longitudinal stability.

Conclusions

Visual image correlation represents a reliable method to obtain the global deformations and rigid body translations of a model during generic tests in wind tunnels, providing high-spatial resolution 3D displacements and strains. An experimental setup was conceived and assembled around a low-speed wind tunnel, integrating VIC and aerodynamic coefficient measurements. A specific procedure was developed for the preparation and testing of flexible wings applied to micro aerial vehicles, and particular care was devoted to the treatment of the specimen to prevent significant reinforcement of the flexible wings. Three wings with the same nominal geometry, but distinct structures were tested: a rigid (R), a batten reinforced (BR), and a perimeter reinforced (PR) wing. Conventional wind tunnel testing for the longitudinal aerodynamic coefficients indicated significant advantages in a flexible membrane wing performance. The three-dimensional wing surface displacements were acquired through the VIC technique for loaded cases and correlated with the corresponding measured aerodynamic coefficients. Substantial geometric twisting of the BR wing, caused by the adaptive washout, was found to improve the stall and displayed a potential inherent resistance to wind gusts. Conversely, dramatic changes with AOA and dynamic pressure in the camber of a PR wing, caused by adaptive membrane billowing, were demonstrated to increase both lift and static longitudinal stability. Current work concerning flexible MAV wings is concerned with model validation, numerical optimization and experimentation involving dynamic considerations.

Acknowledgements This work was supported jointly by the Air Force Research Laboratory and the Air Force Office of Scientific Research under F49620-03-1-0381 with Todd Combs, Sharon Heise and Johnny Evers as project monitors. The authors would also like to acknowledge the technical contributions and funding of Martin Waszak at the NASA Langley Research Center.

References

1. Mueller TJ (ed) (2001) Fixed and flapping wing aerodynamics for micro air vehicle applications. American Institute of Aeronautics and Astronautics, Reston, VA.
2. Zimmerman CH (1935) Aerodynamic characteristics of several airfoils of low aspect ratio, NACA Technical Report TN 539.
3. Winter H (1932) Flow phenomena on plates and airfoils of short span, NACA Technical Report TN 798.
4. Prandtl L, Tietjens OG, Hartjog J (1934) Applied hydro and aeromechanics. McGraw-Hill, London.
5. Hoerner SF (1975) Fluid dynamic lift. Hoerner, Brick Town, NJ.
6. Mueller TJ (1999) Aerodynamic measurements at low Reynolds numbers for fixed wing MAVs, RTO/VKI Special Course on Development and Operation of UAVs for Military and Civil Applications, VKI, Belgium, September.
7. Pellettier A, Mueller TJ (2000) Low Reynolds number aerodynamics of low-aspect ratio, thin/flat/cambered-plate wings. J Aircr 37 (5):825–832.
8. Torres GE, Mueller TJ (2004) Low-aspect ration wing aerodynamics at low Reynolds numbers. AIAA J 45(5):865–873.
9. Ifju PG, Jenkins DA, Ettinger S, Lian Y, Shyy W, Waszak MR (2002) Flexible-wing-based micro air vehicles, AIAA Paper 2002-0705, (January).
10. Ifju PG, EttiZnger S, Jenkins DA, Martinez L (2001) Composite materials for micro air vehicles. In: Proceeding for the SAMPE annual conference, Long Beach CA, (May).
11. Waszak MR, Jenkins LN, Ifju PG (2001) Stability and control properties of an aeroelastic fixed wing micro aerial vehicle, AIAA Paper 2001–f4005, (August).
12. Albertani R, Hubner JP, Ifju PG, Lind R, Jackowski J (2004) Experimental aerodynamics of micro air vehicles, SAE World Aviation Congress and Exhibition, Paper 04AER-8, (November).
13. Albertani R, Stanford B, Hubner JP, Ifju PG (2005) Characterization of flexible wing MAV's: aeroelastic and propulsion effects on flying qualities, AIAA Paper 2005-6324, (August).
14. Lian Y, Shyy W, Ifju PG (2003) Membrane wing model for micro air vehicles. AIAA J 41(12):2492–2494.

15. Lian Y, Shyy W (2003) Three dimensional fluid structure interactions of a membrane wing for MAV applications, AIAA Paper 2003-1726, (April).
16. Fleming GA, Burner AW (1999) Deformation measurements of smart aerodynamic surfaces, SPIE Paper No. 3783-25, 44th Annual SPIE International Symposium on Optical Science, Engineering, and Instrumentation—Optical Diagnostics for Fluids/Heat/Combustion and Photomechanics for Solids, (July).
17. Fleming GA, Bartram SM, Waszak MR, Jenkins LN (2001) Projection Moire interferometry measurements of micro air vehicle wings, SPIE Paper no. 4448-16, (November).
18. Burner AW, Flemming GA, Hoppe JC (2000) Comparison of three optical methods for measuring model deformation, AIAA Paper 2000-0835, January.
19. Spain CV, Heeg J, Ivanco TG, Barrows DA, Florance JR, Burner AW (2004) Assessing videogrammetry for static aeroelastic Testing of a Wind-Tunnel Model, AIAA Paper 2004-1677, (April).
20. Hooker JR, Burner AW, Valla R (1997) Static aeroelastic analysis of transonic wind tunnel models using FE methods, AIAA Paper 97-2243, June.
21. Nassefa HS, Pornsinsirirakb HN, Taib YC, Ho CM (2003) Unsteady aerodynamics and flow control for flapping wing flyers. Prog Aerosp Sci 39:635–681.
22. Pennycuick CJ, Lock A (1976) Elastic energy storage in primary feather shafts. J Exp Biol 64:667–689.
23. Combes SA, Daniel TL (2003) Flexural stiffness in insect wings II. Spatial distribution and dynamic wing bending. J Exp Biol 206:2989–2997.
24. Sutton MA, Cheng M, Peters WH, Chao YJ, McNeill SR (1986) Application of an optimized digital correlation method to planar deformation analysis. Image Vis Comput 4(3):143–151.
25. Sutton MA, Turner JL, Bruck HA, Chae TA (1991) Full field representation of the discretely sampled surface deformations for displacement and strain analysis. Exp Mech 31(2):168–177.
26. Lichtenberger R, Schreier H (2002) Non-contacting measurement technology for component safety assessment, Limess Messtechnik u. Software GmbH, D-75180 Pforzheim, (December).
27. Vic-3D digital image correlation software, correlated solutions, inc., Columbia SC.
28. Sutton MA, McFadden C (2000) Development of a methodology for non-contacting strain measurements in fluid environments using computer vision. Opt Lasers Eng 32:367–377.
29. Albertani R (2005) Experimental aerodynamic and elastic deformation characterization of low aspect ratio flexible fixed wings applied to micro aerial vehicles. Ph.D. Dissertation, Department of Mechanical and Aerospace Engineering, University of Florida, Gainesville, Florida, (December).
30. Lian Y, Shyy W, Three dimensional fluid structure interactions of a membrane wing for MAV applications, AIAA Paper 2003-1726.
31. Albertani R, Boria F, Bowman S, Claxton, Crespo A, Francis C, Ifju P, Johnson B, Jung S, Lee KH, Morton M, Sytsma M (2005) Development of reliable and mission capable micro air vehicles, University of Florida, MAE Dept., 9th International MAV Competition, South Korea.
32. Wainwright SA, Biggs WD, Currey JD, Gosline JM (1976) Mechanical design in organisms. Princeton University Press, Princeton, NJ.